UC Santa Barbara
UC Santa Barbara Previously Published Works

Title

Crystallization of Bottlebrush Statistical Copolymers of Polystyrene and Poly(ethylene oxide)

Authors

Gan, Xuchen

Seong, Hong-Gyu

Hu, Mingqiu

et al.

Crystallization of Bottlebrush Statistical Copolymers of Polystyrene and Poly(ethylene oxide)

Xuchen Gan,[1‡] Hong-Gyu Seong,[1‡] Mingqiu Hu,[1] Zhan Chen,[1] Todd Emrick,[1] and Thomas P. Russell[1,2]*

[1]Department of Polymer Science and Engineering, University of Massachusetts, Amherst, MA 01003

[2]Materials Sciences Division, Lawrence Berkeley National Laboratory, Berkeley, CA 37831

KEYWORDS   Bottlebrush statistical copolymers, Semicrystalline, Microphase separation

ABSTRACT   Bottlebrush statistical copolymers (BSCPs) with poly(ethylene oxide) (PEO) and polystyrene (PS) side chains grafted to a polynorbornene (PNB) backbone were synthesized by ring-opening metathesis polymerization (ROMP). The impact of the glassy PS sidechains on the crystallization of the PEO sidechains as a function of the backbone length, grafting densities, and fraction of the PS and PEO side-chains is described. The bottlebrush architecture, where the side-chains are anchored to the backbone, inherently constrains the mobility of PEO. Compared to the bulk crystallization temperature of PEO, the higher glass transition temperature of PS places further constraints on PEO crystallization. The limited mobility of PEO leads to a cold crystallization behavior during heating. Reduced grafting densities in turn reduce side-chain crowding, leading to less extended pendant structures. The degree of crystallinity of PEO was

23 found to decrease at lower grafting densities to a point where crystallization was not observed.

24 The average distance between bottlebrush backbones increased linearly with the backbone

25 length, suggesting that the backbone forms a distinct mesodomain. For BSCPs with asymmetric

26 volume fractions of PS and PEO side-chains, the degree of crystallinity of PEO increases with a

27 change from cold crystallization to normal nucleation and growth during cooling, as a result of

28 reduced constraints on PEO mobility by the glassy PS sidechains.

29

30 **INTRODUCTION** With advances in controlled polymerization and catalyst optimization,

31 bottlebrush polymers (BPs) can now incorporate a wide range of segments having unique

32 architectures, composition and functionality, affording exceptional opportunities to manipulate

33 self-assembly and phase transition behavior[1–5]. BPs have been used as photonic crystals,[6–9]

34 elastomers,[13–15] surfactants,[13–17] batteries,[18,19] drug delivery,[20] and for patterning.[21–23] The high

35 density of chains anchored to a linear backbone massively reduces, if not eliminates, inter-

36 bottlebrush entanglements, significantly enhancing the dynamics of the bottlebrush block

37 copolymers (BBCPs) in the bulk, as manifest in the rapid microphase separation with a repeat

38 period in the direction of the backbone.[24–26] For bottlebrush statistical copolymers (BSCPs),

39 where the two side chains are randomly distributed along the backbone, the repeat period is

40 orthogonal to the backbone with the side extending out on different sides of the backbone. Thus,

41 the domain size of BBCPs is determined by backbone length, while that of BSCPs depends upon

42 the side chain length. Such polymers with advanced architectures, including star block

43 copolymers and bottlebrush core-shell block copolymers, can exhibit unique phase behavior.[27–29]

44   Poly (ethylene oxide) (PEO) is a semi-crystalline, water-soluble polymer of considerable

45   interact for its crystallization properties under various states of confinement.[30–32] Linear

46   polystyrene-*block*-PEO adopts the same crystalline structure as PEO but the crystallization and

47   melting temperatures are depressed due to confinement by the glassy PS microdomain.[33] For

48   PEO bottlebrush homopolymers, the constraint arising from the polynorbornene (PNB) backbone

49   restricts PEO mobility, resulting in a decreased spherulite growth rate and size.[34] The sequence

50   and ratio of amorphous poly(propylene oxide) (PPO) and semi-crystalline PEO in PPO-PEO

51   core-shell BBCPs greatly affect the overall crystallization and phase behavior.[29] For BSCPs with

52   PDMS and PEO side chains, where the glass transition temperature (T_g) of PDMS is much lower

53   than the crystallization temperature of PEO, PEO crystallization disrupts the lateral order of the

54   self-assembled lamellar morphology of the two side-chains, and the PNB backbone loops

55   between the two side-chain domains to form a third backbone mesodomain.

56   Here we describe BSCPs with PS and PEO side-chains, where the backbone constrains the

57   mobility of PEO side chains, and the PS microdomains with a T_g higher than the crystallization

58   temperature of PEO adds additional confinement constraints. This frustrates the mobility of the

59   PEO chains by 1) fixing the chain end to the backbone and 2) prohibits the movement of PEO

60   chains by the glassy and solid-like domains formed by PS. To understand the crystallization and

61   microphase behaviors of PS-PEO BSCPs, we synthesized three types of polymers: 1) fully

62   grafted BSCPs with different backbone lengths; 2) BSCPs with different grafting densities at

63   fixed backbone chain lengths; and 3) BSCPs with different PS and PEO side-chain ratios at fixed

64   backbone length and grafting density. The fully grafted samples are prepared by ROMP of

65   norbornene-terminated PEO and PS macromonomers, while the loosely grafted samples have

66   *cis*-5-norbornene-*exo*-2,3-dicarboxylic anhydride spacer units. Differential scanning calorimetry

67 (DSC) and small- and wide-angle X-ray scattering (SAXS and WAXS) were used to characterize

68 the crystallization and phase behavior.

69

70 **EXPERIMENTAL SECTION**

71 *Materials*

72 Propagylamine (98%), 6-aminohexanoic acid ($\geq$ 98.5%), *N,N′*-dicyclohexylcarbodiimide (99%,

73 DCC), 4-(dimethylamino)pyridine (ReagentPlus®, $\geq$ 99%, DMAP), triethylamine ($\geq$ 99%,

74 TEA), ethyl vinyl ether ($\geq$ 99%, EVE), Grubbs Catalyst M204, pyridine anhydrous (99.8%),

75 sodium azide (ReagentPlus®, $\geq$ 99.5%, NaN_3), *N,N*-dimethylformamide (anhydrous, 99.8%,

76 DMF), ethyl *α*-bromoisobutyrate (98%, EBiB), styrene (ReagentPlus®, 99.9%) copper (I)

77 bromide (98%, $Cu^I Br$), *N,N,N′,N″,N″*-pentamethyldiethyltriamine (99%, PMDETA),

78 tetrahydrofuran (anhydrous, $\geq$ 99.9%, inhibitor-free, THF) and poly(ethylene glycol) methyl

79 ether (average M_n ~ 2,000 Da, flakes) were purchased from Sigma Aldrich. *Cis*-5-norbornene-

80 *exo*-2,3- dicarboxylic anhydride was purchased from Oakwood Chemical. Toluene (certified

81 ACS, $\geq$ 99.5%), methanol (certified ACS, $\geq$ 99.8%, MeOH), hexane (certified ACS, $\geq$ 98.5%),

82 ethyl acetate (certified ACS, $\geq$ 99.5%), acetone (certified ACS, $\geq$ 99.5%), methylene chloride

83 (stabilized, certified ACS, $\geq$ 99.5%), diethyl ether (anhydrous, BHT stabilized/certified ACS,

84 $\geq$ 99%), hydrochloric acid (certified ACS plus, 36.5 to 38.0%), sodium sulfate (anhydrous,

85 granular/certified ACS, $\geq$ 99.0%), and sodium bicarbonate (powder/certified ACS, 99.7 to

86 100.3%) were purchased from Fisher Scientific. Deuterated chloroform ($CDCl_3$) for NMR

87 spectroscopy was purchased from Cambridge Isotope Laboratories. DCM and TEA were purified

88 by distillation over calcium hydride. THF was purified by distillation over sodium benzophenone

89 ketyl.

General procedure for ROMP of macromonomers – (PS-PEO)$_{N_{BB}}$

91 In a typical experiment, **NB-PS** (130 mg, 0.05 mmol) and **NB-mPEO** (125 mg, 0.05 mmol)

92 were charged in a flame-dried 20 mL scintillation vial with a magnetic stirring bar. The vial was

93 purged with $N_{2(g)}$ and anhydrous THF (1.5-1.95 mL, final [MM] upon injection of G3 stock

94 solution were targeted at 0.05 M) was added to the vial. In another flame-dried 7 mL scintillation

95 vial, a stock solution of initiator (G3, 0.01 M) was prepared under $N_{2(g)}$ atmosphere. The

96 polymerization was initiated by adding the G3 stock solution to the macromonomer solution in

97 stoichiometric amounts intended to yield a desired N_{BB} = [MMs]:[G3]. The solution was stirred at

98 room temperature under $N_{2(g)}$ for 2 h. Ethyl vinyl ether (0.1 mL) was added to quench the

99 polymerization. The crude products were dried under vacuum to yield a pale brown powder in

100 high conversion (~95%) and yield (>98%).

Size-Exclusion Chromatography (SEC)

102 SEC in THF was performed at 40 °C at a flow rate of 1.0 mL min^{-1} on an Agilent 1260 infinity

103 system with a G1362A refractive index detector and G1310B isocratic pump, equipped with a

104 PLgel 5 μm mixed-c (7.5 mm × 300 mm), a PLgel 5 μm mixed-d (7.5 mm × 300 mm), and a 5

105 μm guard column (7.5 mm × 50 mm) calibrated against polystyrene (PS) standards. Multiangle

106 laser light scattering (MALLS) SEC of the bottlebrush polymers was carried out in THF with 1

107 vol % of TEA at 30 °C on two PLgel 10 μm mixed bed columns and two detectors: MALLS and

108 differential refractive index (dRI) at a flow rate of 1.0 mL min^{-1}. For SEC analysis, the polymers

109 were first dissolved in THF (3.0 mg mL^{-1}) and then passed through a 0.45 μm

polytetrafluoroethylene (PTFE) filter. The differential refractive index (*dn/dc*) was obtained for each sample assuming 100% mass recovery. The number-average molar mass (M_n) and polydispersity index (PDI) were determined by constructing a partial Zimm plot for each slice of the elution profile.

Nuclear Magnetic Resonance (NMR) Spectroscopy

^{1}H and ^{13}C NMR spectra were recorded on a Bruker Avance-500 spectrometer operating at 500 and 126 MHz, respectively, and chemical shifts reported in ppm were calibrated to residual solvent signals.

Differential Scanning Calorimetry (DSC)

The crystallization behavior of the PS-PEO BSCPs is measured and characterized by DSC (TA Q200 with RCS90 device). Polymers are firstly heated from room temperature to 120°C at the heating rate of 10°C min^{-1} and held for 5 minutes to remove the thermal history. Then, the temperature is decreased to -50°C and increased to 120°C in exothermic and endothermic cycles at 8°C min^{-1}.

Small- and Wide-Angle X-ray Scattering (SAXS and WAXS)

X-ray scattering measurements are performed on an in-house Ganesha SAXS-LAB facility with Cu K☐ radiation (wavelength ☐ = 0.1542nm) and a 2D area detector (Pilatus 300K). The original scattering images are processed and analyzed with the python package XRayScatter.py (https://github.com/mingqiuhu/XRayScatterPy) developed by Hu et al.[36]. For the in-situ small- and wide-angle X-ray Scattering (SAXS and WAXS) at different temperatures, the polymer sample temperature is controlled between -50°C and 100°C using a Linkam sample stage. All samples are thermally annealed at 150°C for 12 hours before X-ray measurements.

RESULTS AND DISCUSSION

Synthesis of BSCPs

Norbornene dicarboximide-linked macromonomers containing poly(ethylene oxide monomethyl ether) (**NB-mPEO**) were synthesized by esterification of mPEO with *N*-(carboxyhexyl)-*cis*-5-norbornene-*exo*-2,3-dicarboxyimide.[35] The polystyrene-based macromonomer (**NB-PS**) was synthesized by copper-catalyzed azide-alkyne cycloaddition of PS-N$_3$ with the corresponding NB-alkyne (*N*-(propargyl)-*cis*-5-norbornene-*exo*-2,3-dicarboxyimide), in which PS-N$_3$ was prepared by atom-transfer radical polymerization of styrene followed by conversion of the alkyl bromide chain-end to azide with NaN$_{3(s)}$.[16] Macromolecular synthesis and characterization are given in the Supporting Information. Subsequently, BSCPs with PS and PEO side chains were synthesized by ruthenium benzylidene-initiated ROMP, utilizing G3 as the initiator (**Figure 1a**). The backbone degree of polymerization (N_{BB}) was modulated by adjusting the [macromonomers]:[G3] ratio. MALLS-SEC traces (**Figure 1c**) are indication of successful ROMP at over a range of targeted N_{BB} values (from 20 to 200), with a marked shift in peak position shorter retention time at higher target N_{BB}. High conversion was evidenced by the nearly complete depletion of SEC signals associated with macromonomers (both **NB-PS** and **NB-mPEO**) ~16.8-18.8 min. Quantification of the side-chain ratio was accomplished using ^{1}H nuclear magnetic resonance (NMR) spectroscopy by comparing the peak integration of PS at 6.25-7.25 ppm (br, -$\underline{C_6H_5}$) and the PEO at 3.64 ppm (s, -$\underline{CH_2CH_2}$O-). Detailed procedures for data processing and corresponding results are provided in the Supporting Information and **Table 1**, respectively. Further experiments involved varying the

154   **NB-PS** molar ratio from 40 to 0% while maintaining N_{BB} at 200. Due to the similar molecular

155   weights of the two macromonomers, the peak positions of the resulting polymers remained

156   almost constant (13.9-14.0 min), indicating consistent molecular weights (**Figure 1d**). The

157   grafting densities of the BSCPs, at a fixed N_{BB} of 200 and PS:PEO molar ratio of 1:1, were

158   adjusted by copolymerizing *cis*-5-norbornene-*exo*-2,3-dicarboxylic anhydride (**NB**) as a spacer to

159   increase the average inter-side-chain distances (**Figure 1b**). Successful ROMP is depicted in

160   **Figure 1e**, where lower molecular weights were observed at lower grafting densities, attributed

161   to a decreased number of polymeric side chains per BSCP. Significant peak broadening at lower

162   retention times was observed with reduced grafting density, likely arising from to the decreased

163   solubility of the BSCPs due to the higher **NB** mol %, that would compromise ROMP control.

164   This was evident from the precipitation observed during the control experiment of **NB**

165   homopolymerization (**Figure S5**). Efforts to quantify the grafting density were unsuccessful due

166   to the overlap of vinyl protons in norbornene for macromonomers and **NB**, occurring at

167   approximately 6.28 ppm. Detailed synthetic procedures and characterization outcomes for

168   bottlebrush statistical copolymer synthesis are shown in Supporting Information.

169

170
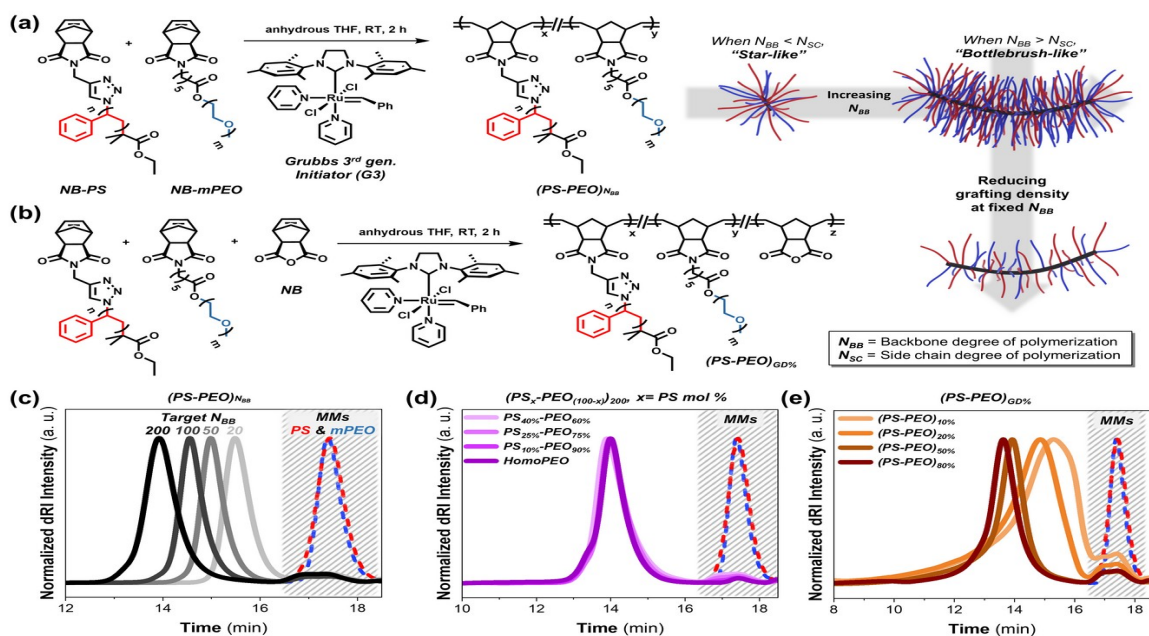
Figure 1. (a) ROMP of **NB-PS** and **NB-mPEO**, and illustrations of bottlebrush statistical copolymer shapes as a function of N_{BB}; (b) ROMP of **NB-PS**, **NB-mPEO** and **NB**, and illustrations of a BSCP with reduced grafting density; MALLS-SEC traces of different (c) N_{BB}, (d) macromonomer ratio, and (e) grafting density (Z) of BSCPs.

175

Table 1. Characterization data for BSCPs.

Entry	Target N_{BB} ([MMs]/[G3])	Target Z (%)	Target PEO ratio (%)	Target PS ratio (%)	PEO ratio (%)	PS ratio (%)	$M_{n,}$ theo (kDa)	M_n (kDa)	M_w (kDa)	PDI
(PS-PEO)$_{200}$	200	100	50	50	51.4	48.6	510.0	589.9	802.0	1.36
(PS-PEO)$_{100}$	100	100	50	50	50.9	49.1	255.0	270.8	334.3	1.24
(PS-PEO)$_{50}$	50	100	50	50	51.0	49.0	127.5	139.7	173.9	1.25
(PS-PEO)$_{20}$	20	100	50	50	50.3	49.7	51.0	61.5	74.9	1.22
PS$_{40\%}$-PEO$_{60\%}$	200	100	60	40	60.4	39.6	508.0	472.0	652.1	1.38
PS$_{25\%}$-PEO$_{75\%}$	200	100	75	25	76.0	24.0	505.0	467.0	606.3	1.30

PS$_{10\%}$-PEO$_{90\%}$	200	100	90	10	91.0	9.0	502.0	406.4	530.0	1.30
HomoPEO	200	100	100	0	100	0	500.0	398.2	525.6	1.32
(PS-PEO)$_{80\%}$	200	80	50	50	50.9	49.1	414.6	546.5	742.3	1.36
(PS-PEO)$_{50\%}$	200	50	50	50	50.7	49.3	271.4	298.0	405.4	1.36
(PS-PEO)$_{20\%}$	200	20	50	50	51.3	48.7	128.2	168.7	217.6	1.29
(PS-PEO)$_{10\%}$	200	10	50	50	51.6	48.4	80.5	487.6	554.3	1.14

177

178   All side-chains of the same chemical structures have the same side-chain length (N_{sc}) and same
179 molecular weight (M_n). $M_{n,\,SEC}$ (PEO) = 2.5 kDa; $M_{n,\,SEC}$ (PS) = 2.6 kDa; $M_{n,\,SEC}$ (PDMS) = 2.7
180 kDa. The side-chain ratio was calculated based on ^{1}H NMR spectroscopy.

181

182 ***Fully Grafted Symmetric PS-PEO BSCPs***

183   The impact of constraint from the glassy PS sidechains on PEO crystallization was assessed by

184 comparing fully grafted PS-PEO BSCPs and our previously reported PDMS-PEO BSCPs, where

185 the latter has no such constraint due to the low T_g of the PDMS component. As shown in the

186 DSC cooling and heating curves in **Figure 2a**, the PEO side chains in (PDMS-PEO)$_{200}$

187 crystallized at 14 °C during cooling and melted at 47 °C during heating, similar to that of

188 unconstrained PEO homopolymers. However, for (PS-PEO)$_{200}$, no crystallization was observed

189 during cooling (**Figure 2b**), suggesting that the PEO chains, under the constraint of glassy PS,

190 lack the mobility to organize into a crystal lattice. Instead, a broad exotherm is seen during

191 heating, followed by the melting of PEO crystallites at 42 °C. This broad exotherm has an

192 integrated area close to that of the subsequent endothermal melting peak, indicating that the PEO

193 side-chains in the fully grafted (PS-PEO)$_{200}$ BSCPs undergo a *cold crystallization* during the

194 quench-and-reheat cycle. The degree of crystallinity, X_c of PEO, was calculated using the ratio

195 between the melting peak area in the DSC endothermic cycles and the standard melting enthalpy

196 of PEO (205 J/g) normalized by the weight percentage of PEO in the BSCPs. X_c of (PDMS-

197 PEO)$_{200}$ was 47% and X_c of (PS-PEO)$_{200}$ was 25%, indicating that the confinement from glassy PS

198 side-chains reduces the degree of crystallinity of the PEO sidechains in PS-PEO BSCPs.

199   Temperature dependent small- and wide-angle X-ray scattering (SAXS and WAXS) was used

200 to correlate PEO crystallization to the BSCP morphologies. SAXS gives morphological

201 information on the tens-of-nanometer nm-scale, while WAXS monitors the local ordering of

202 PEO. For (PS-PEO)$_{200}$ in **Figure 2c,** the WAXS shows a similar cold crystallization during

203 cooling and re-heating. Before cooling, the WAXS of the original BSCPs consisted mainly of a

204 diffuse halo arising from the amorphous interchain separation distance of the PS and PEO

205 sidechains. Weak interferences from more ordered PEO are evident as shoulders on the diffuse

206 halo. No obvious crystallization was observed when the BSCPs were cooled to -50 °C from

207 room temperature. The sharp diffraction peaks at scattering vectors of ~1.33Å^{-1}, 1.61Å^{-1}, and

208 1.84Å^{-1} are seen due to the monoclinic crystal structure of PEO[33] that forms during reheating

209 from -50 °C to 20 °C. The onset of cold crystallization during heating matches the DSC results,

210 further confirming the constraint of PEO mobility by glassy PS sidechains.

211   The SAXS profiles characterize the morphology of the BSCPs. Compared with our previous

212 study of PDMS-PEO BSCPs, which self-assembled into a laterally ordered lamellar morphology

213 with melted PEO, the disorder of the PS-PEO BSCPs is evidenced by the absence of any

214 characteristic SAXS reflections at 80 °C. Unlike BBCPs, where microphase separation is

215 enforced by connecting various sidechains to different sections of the backbone, microphase

216 separation of BSCPs relies on the chemical disparity between the two sidechains, like linear

217 diblock copolymers. ꭓ for PS and PEO at room temperature is 0.076[36,] and for PDMS and PEO is

218 0.22[37]. For linear diblock copolymers with symmetric volume fractions of the two blocks, the

219   order-disorder transition occurs at $\chi N=10.5$[38,39], corresponding to a volume-averaged degree of

220   polymerization of 138 and 48 for PS-PEO and PDMS-PEO, respectively. Compared with our

221   previous study on PDMS-*stat*-PEO that is microphase-separated with $\chi N=14.86$, PS-PEO having

222   a similar molecular weight is phase mixed, due to the smaller χ value, in agreement with the

223   SAXS results at 80 °C in **Figure 2c**. The χN of PS-PEO is calculated to be 4.79, using 118 $\mathring{A}^3$ as

224   the reference volume. Despite predictions by self-consistent field theory calculations that

225   connecting sidechains to a bottlebrush backbone would enhance the degree of segregation at the

226   same χN[40,41], 4.79 is insufficient for microphase separation. As a result, besides the constraint

227   from the glassy PS sidechains, the phase-mixed morphology also contributes to the decreased X_c

228   and cold crystallization of PEO sidechains in PS-PEO BSCPs.

229   A scattering peak at ~0.12 $\mathring{A}^{-1}$ is observed for all the BSCPs. The scattering is most

230   pronounced with amorphous or melted PEO sidechains, for example, before cooling or after

231   heating above the melting temperature. The scattering weakens when the PEO crystallizes, as

232   shown in the SAXS profiles from -20 °C to 40 °C during cold crystallization. The correlation

233   distance of this scattering is 5.2 nm. In our previous study of PDMS-PEO with similar molecular

234   weight, the full pitch of microphase-separated lamellar morphology is 13.5 nm, with an inter-

235   backbone distance being half of the full pitch, 6.8 nm. We attribute the 5.2 nm correlation

236   distance in SAXS of PS-PEO BSCPs to the inter-backbone distance. It is understandable that the

237   inter-backbone distance of phase mixed PS-PEO BSCPs is smaller than microphase separated

238   PDMS-PEO BSCPs with similar molecular weights. That the scattering is most pronounced

239   without PEO crystallization and weakens upon PEO crystallization is attributed to disruption of

240 backbone conformation when PEO crystallizes. This is similar to our observations on PDMS-

241 PEO BSCPs, where PEO crystals disrupt the lateral order of self-assembled morphologies.

242 Another significant feature in the SAXS profile occurs at ~0.028 Å^{-1}, where scattering was

243 evident in the BSCPs before quenching and remained unchanged during cold crystallization until

244 melting at 70 °C. A shoulder emerged to the right of this scattering ~0.05 Å^{-1} when the BSCPs

245 were quenched and then reheated to allow the cold crystallization to proceed. The shoulder

246 disappeared between 40 °C and 50 °C. We attribute the scattering at ~0.028 Å^{-1} to PEO

247 crystallites in the BSCPs before quenching, likely due to heterogeneous nucleation during

248 sample preparation. This scattering remained unchanged during quenching and reheating,

249 without crystal growth, further confirming that PEO crystallization is hindered by glassy PS

250 sidechains. The emergence of the shoulder at a scattering vector higher than that of the original

251 scattering during reheating, and its disappearance between 40 °C and 50 °C, match the cold

252 crystallization observed by DSC with a melting temperature of 45 °C. This suggests that a

253 homogeneous nucleation occurred during quenching, while the crystal growth during subsequent

254 heating yielded crystallites with smaller inter-crystallite distances than previously existing

255 crystallites. The crystallites grown during cold crystallization first melted during heating, after

256 which the scattering curves at 50 °C and 60 °C were similar to those at 20 °C before quenching

257 and reheating. Subsequently, the crystallites from heterogeneous nucleation fully melted above

258 60 °C, and the phase-mixed BSCPs showed no obvious SAXS peaks at 70 °C and 80 °C.
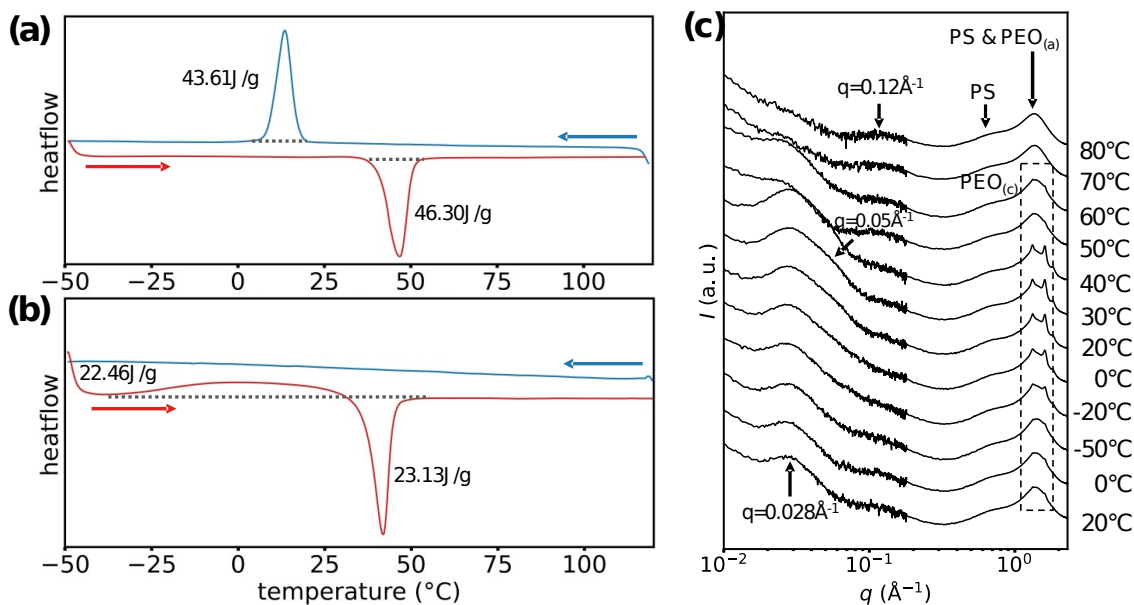
Figure 2. (a) and (b) DSC curves of fully grafted symmetric $(PDMS-PEO)_{200}$ and $(PS-PEO)_{200}$ BSCPs. The endothermic and exothermic cycles are measured within the temperature range of -50 °C to 120 °C at a heating and cooling rate of 8 °C min^{-1}. (c) Small-angle and wide-angle X-ray scattering intensity as a function of the scattering vector (q) of $(PS-PEO)_{200}$ during cooling and reheating. $PEO_{(a)}$ and $PEO_{(c)}$ refers to amorphous and crystalline PEO respectively. The X-ray profiles are vertically shifted for clarity.

To evaluate the impact of the backbone degree of polymerization on PEO crystallization, PS-PEO BSCPs were synthesized with symmetric ratios of the two side-chains over a range of N_{BB} from 20 to 200. The broad, diffuse WAXS interference maximum indicates that the PEO sidechains were amorphous before quenching and reheating, regardless of N_{BB}. The WAXS reflections characteristic of the crystalline structure of PEO appear after quenching and reheating, with similar intensities for BSCPs of different backbone lengths. From the WAXS data, we conclude that cold crystallization and the X_c of PEO are independent of N_{BB}. Also, the inter-backbone distance, indicated by the peak at ~ 0.12 Å^{-1}, did not depend on N_{BB}, and it weakened after PEO cold crystallization, similar to that shown in Figure 2. SAXS shows either no peaks or weak peaks before quenching and reheating, further confirming that the BSCPs were

14

277 phase-mixed with no crystalline PEO domains before cold crystallization. After quenching and

278 reheating, the intense SAXS halo, highlighted by the dashed rectangle SAXS, corresponds to

279 intercrystallite distance associated with PEO cold crystallization. The peak position decreases

280 with increasing N_{BB}, suggesting an increase in the distance between neighboring crystallites. This

281 is not observed in going from $N_{BB} = 10$ to 50 and is only observed for BSCPs of larger N_{BB}. For

282 the fully grafted BBCPs, the side-chains are more extended than linear polymers, due to side-

283 chain crowding. However, we note that the sidechain crowding is only significant when the

284 bottlebrush backbone is longer than the sidechains.[40,41] With a short backbone, the free space at

285 both ends of the backbone reduces the bulkiness of sidechain packing. For the PS-PEO BSCPs in

286 this study, with side-chain degree of polymerization (N_{SC}) of ~35, the transition of side-chain

287 packing bulkiness is expected to occur above 35, the same range where the inter-crystallite

288 distance increases. Consequently, we conclude that crowded side-chains increase the distance

289 between nearby PEO crystallites, likely due to larger crystallites.
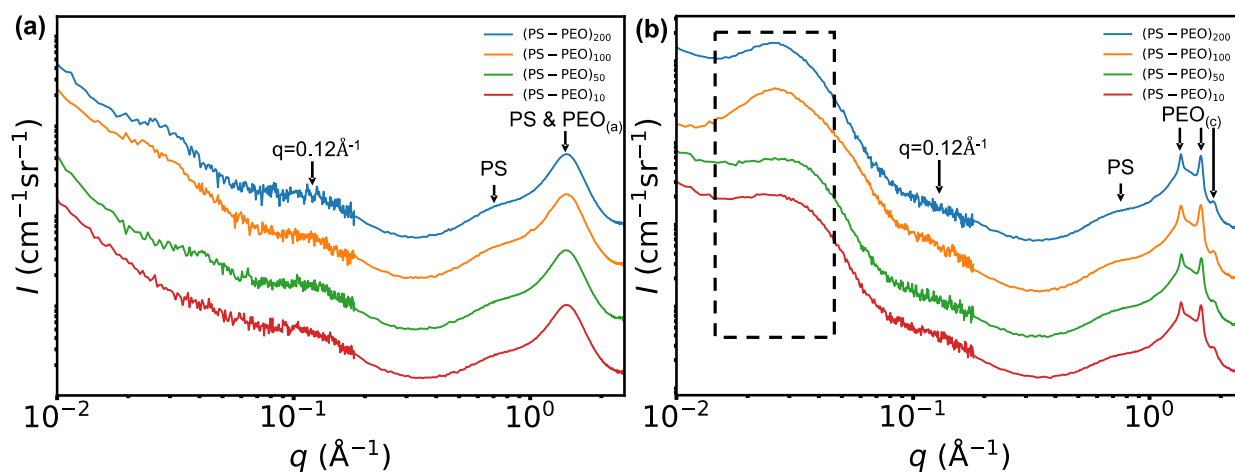
Figure 3. The absolute 1D X-ray scattering intensity profiles of (a) fully grafted symmetric PS-PEO BSCPs before thermal annealing and (b) the same samples then annealed and quenched to -50°C and reheated to room temperature. The dashed rectangle refers to the SAXS peak corresponding to inter-molecular distance. The X-ray profiles are shifted vertically for clarity.

296 *Loosely Grafted Symmetric PS-PEO BSCPs*

297   The impact of grafting density on PEO crystallization and microphase separation between the

298 backbone and sidechains were examined using loosely grafted PS-PEO BSCPs. A series of

299 symmetric BSCPs was studied with the same backbone length (N_{BB} = 200) but different grafting

300 densities (ranging from 100% to 10%). From the DSC curves in **Figure 4a**, the PEO of loosely

301 grafted BSCPs at a grafting density of 80% exhibits cold crystallization behavior, like the fully

302 grafted BSCPs. As the grafting density decreases from 100% to 80%, the X_c of PEO decreases

303 drastically from 25% to 5%. Upon further decrease of the grafting density to 50% or lower, PEO

304 did not crystallize.

305   The SAXS data in **Figure 4b** shows that the peak corresponding to the inter-backbone distance

306 shifted from 0.12 Å^{-1} to 0.036 Å^{-1} when the grafting density decreased from 100% to 10%. The

307 inter-backbone distance was calculated using Bragg's Law, $d = 2\textrm{p}/q$, and is shown as a function

308 of the number of backbone segments (n) between two nearby sidechains in **Figure 4c**. For

309 example, in fully grafted BSCPs, the number of backbone segments between two adjacent

310 sidechains is 0, since each backbone segment is connected to a sidechain. For a BSCPs with a

311 grafting density of 10%, there are, on average, 9 backbone units between two adjacent side-

312 chains. Surprisingly, a linear relationship is observed between the inter-backbone distance and

313 the number of backbone segments between two adjacent sidechains, as shown in **Figure 4c**. This

314 suggests that the contour length of the backbone segments between two nearby side-chains

315 increases linearly with N_{BB}, which points to fully extended backbone segments, as shown in

316 **Figure 4d**. In our previous study on PDMS-PEO, we concluded that the microphase separation

317 between two side-chains resulted in a backbone stitching, or looping back and forth between two

318 side-chain domains. Here, the linearity observed in **Figure 4c** indicates that the backbone

319 stitches, even without side-chain microphase separation. The forced stitching of the backbone is

320 essential for the side-chains to fill the space as required by incompressibility.[1,38] The backbone

321 forms a distinct mesodomain, contributing to the increasingly intense scattering in the SAXS

322 regime in **Figure 4b** and the increasing distance between two nearby backbones. Despite the

323 backbone stitching, the side-chain packing bulkiness nonetheless decreases at lower grafting

324 density. The reduced sidechain extension contributes to the reduced degree of crystallinity, like

325 our previous study of PDMS-PEO BSCPs.

326
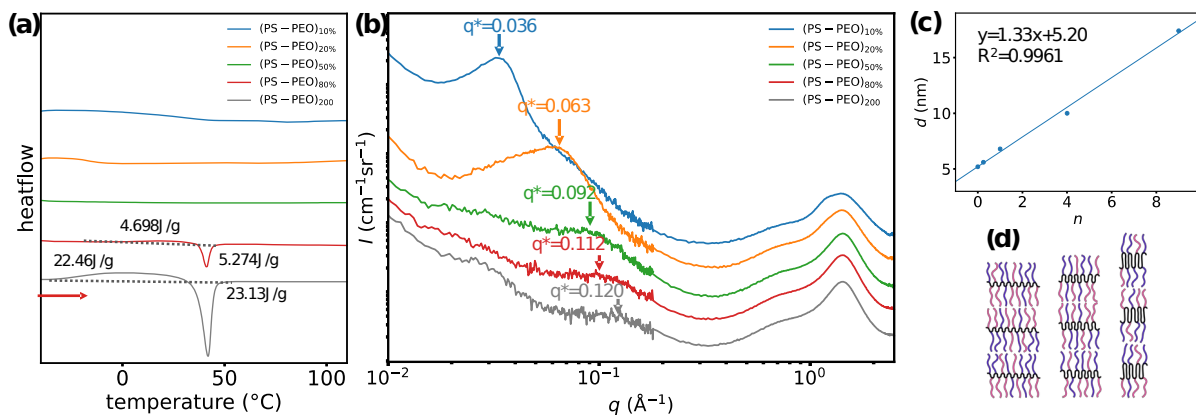
Figure 4. (a) Heating curves for various $N_{BB} = 200$ symmetric PS-PEO BSCPs with different
grafting density. (b) Absolute 1D X-ray scattering intensity profiles of the BSCPs with different
grafting density. The DSC curves and X-ray intensity profiles are vertically shifted for clarity.

330

Fully Grafted Asymmetric PS-PEO BSCPs

332 The impact of the volume ratio between the PS and PEO sidechains in BSCPs on PEO

333 crystallization was evaluated with PS-PEO BSCPs with the backbone length (N_{BB}) fixed at 200.

334 Fully grafted BSCPs were used to ensure side-chain crowding so as to favor crystallization. The

335 DSC curves in **Figure 5a** showed that the increase in PEO volume fraction changed the BSCPs

336 from cold crystallization to traditional nucleation and growth during cooling, as a result of the

337   alleviated constraint from glassy PS sidechains. The degree of crystallinity of PEO also increased

338   from 25% to 50% when the PEO volume ratio increased from 50% to 90%, confirming the

339   relaxation of the constraint on PEO crystallization.

340   Comparing the SAXS and WAXS results in **Figure 5c** of asymmetric PS-PEO BSCPs with

341   **Figure 2** of the symmetric BSCPs, at room temperature before quenching and reheating there is

342   an absence of PEO crystallites for the asymmetric BSCPs. This indicates that the reduced

343   volume ratio of glassy PS leads to reduced heterogeneous crystallization in the as-prepared

344   samples. For $PS_{40\%}$-$PEO_{60\%}$ as shown in **Figure 5c**, the BSCPs at room temperature showed fully

345   amorphous PS and PEO by WAXS, with a diffuse interference maximum at ~0.12Å^{-1}

346   corresponding to the inter-backbone distance, and a broad diffuse halo in the SAXS regime at

347   ~0.012 Å^{-1} arising from the average distance between the PS-rich and PEO-rich domains in the

348   disordered BSCPs. Upon quenching and reheating, the PEO sidechains crystallized, giving rise

349   to WAXS reflections at 1.33Å^{-1}, 1.61Å^{-1}, and 1.84Å^{-1} in the WAXS regime. Also, for $PS_{40\%}$-

350     $PEO_{60\%}$, a peak in the SAXS is seen at 0.07Å^{-1} that shifted to 0.04Å^{-1} during reheating from -20

351   °C to 40 °C. This peak corresponds to the inter-crystallite distance during cold crystallization.

352   Since the SAXS reflections arise from spatial correlations in the electron density, we attribute the

353   abrupt shift from ~ 0.07Å^{-1} to 0.04 Å^{-1} between 30 °C and 40 °C to merging of crystallites. After

354   heating above the melting temperature of PEO crystallites, the SAXS and WAXS curves were

355   almost indistinguishable compared to the that at room temperature before quenching and

356   reheating, confirming the absence of PEO crystallites in disordered BSCPs. Similar to

357   symmetric BSCPs, PEO side-chains crystallization disrupted the backbone conformation as

358   evidenced by the disappearance of the peak at ~0.12Å^{-1} during crystal growth. For the SAXS and

359 WAXS of $PS_{25\%}$-$PEO_{75\%}$ (**Figure 5d**), the features are similar to those in $PS_{40\%}$-$PEO_{60\%}$, with a

360 gradual decrease of the inter-crystallite distance during crystal growth, as shown in the dashed

361 rectangle.
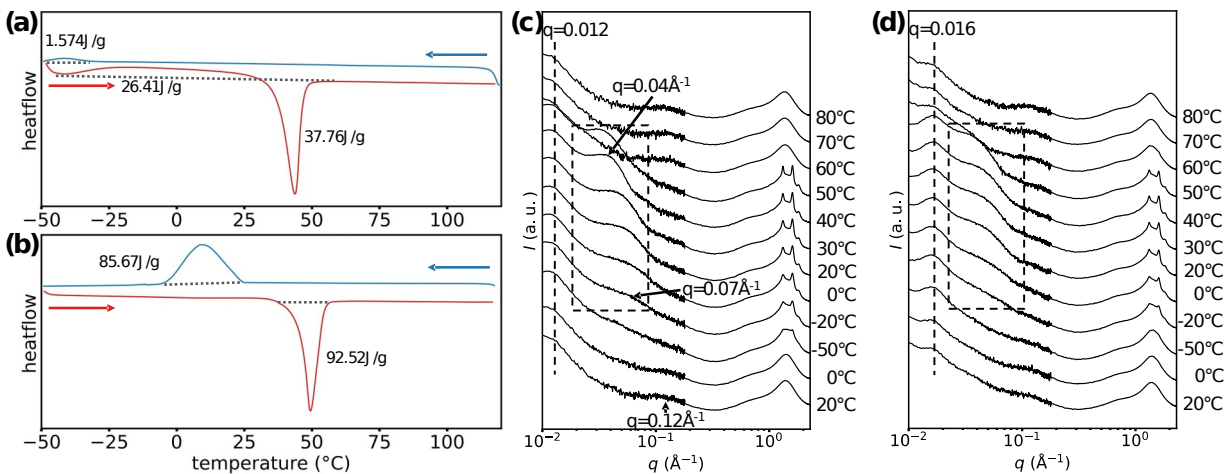
363 **Figure 5.** DSC curves and one-dimensional X-ray scattering profiles of $N_{BB} = 200$ fully grafted
364 asymmetric PS-PEO BSCPs. The DSC exothermic and endothermic cycles for (a) $PS_{40\%}$-$PEO_{60\%}$
365 and (b) $PS_{10\%}$-$PEO_{90\%}$ BSCPs are measured within the temperature range from -50°C to 120°C.
366 1D relative X-ray scattering intensity profile of (c) $PS_{40\%}$-$PEO_{60\%}$ sample and (d) $PS_{25\%}$-$PEO_{75\%}$
367 during its crystallization process. The DSC curves and X-ray profiles are vertically shifted for
368 clarity.

369

370 **CONCLUSION**

371   Using ROMP of **NB-PS**, **NB-mPEO**, and **NB**, we synthesized three types of bottlebrush

372 statistical copolymers (BSCPs). The backbone length, grafting density, and side-chain ratios

373 were tuned to investigate the confinement effect on PEO crystallization and morphology of

374 BSCPs. The BSCPs were phase-mixed when PEO was melted, due to the low cN between PS

375 and PEO. The fully grafted symmetric PS-PEO underwent cold crystallization due to

376 confinement from glassy PS sidechains. The BSCPs did not crystallize during cooling but did

377 crystallize during subsequent heating. Increasing the backbone degree of polymerization

378 facilitated PEO crystallization, as side-chain crowding increases resulting in their extension. As

379 the grafting density decreased, X_c of the PEO decreased, and the distance between adjacent

380 bottlebrush backbones increased. The decreasing X_c of PEO is attributed to less extended side-

381 chains at lower grafting density. The inter-backbone separation distance increased linearly with

382 the number of backbone segments between two adjacent sidechains, suggesting that fully

383 extended backbone segments form distinct backbone mesodomains. By decreasing the PS side

384 chain ratio, PEO has increased the degree of crystallinity and transitioned from cold

385 crystallization during heating to traditional nucleation and growth during cooling.

386

387 **ASSOCIATED CONTENT**

388 Electronically available **Supporting Information** is provided.

389 **AUTHOR INFORMATION**

390 **Corresponding Author**

391 *Thomas P. Russell, email address: russell@mail.pse.umass.edu

392 **Author Contributions**

393 The manuscript was written through contributions of all authors. All authors have given approval

394 to the final version of the manuscript. ‡Xuchen Gan and Hong-Gyu Seong contributed equally to

395 this work.

402 **ABBREVIATIONS**

403 ROMP, ring-opening metathesis polymerization; BP, bottlebrush polymers; BSCP, bottlebrush

404 statistical copolymer; BBCP, bottlebrush block copolymer; PS, polystyrene; PEO, poly (ethylene

405 oxide); PDMS, polydimethylsiloxane; PNB, polynorbornene; PPO, poly (propylene oxide);

406 DSC, differential scanning calorimetry; SAXS, small angle X-ray scattering; WAXS, wide angle

407 X-ray scattering; X_c, degree of crystallinity.

408 **REFERENCES**

409 (1) Rubinstein, M.; Colby, R. H. *Polymer Physics*; OUP Oxford, 2003.
410 (2) Xia, Y.; Olsen, B. D.; Kornfield, J. A.; Grubbs, R. H. Efficient Synthesis of Narrowly
411   Dispersed Brush Copolymers and Study of Their Assemblies: The Importance of Side
412   Chain Arrangement. *J. Am. Chem. Soc.* **2009**, *131* (51), 18525–18532.
413 (3) Kawamoto, K.; Zhong, M.; Gadelrab, K. R.; Cheng, L.-C.; Ross, C. A.; Alexander-Katz, A.;
414   Johnson, J. A. Graft-through Synthesis and Assembly of Janus Bottlebrush Polymers from
415   A-Branch-B Diblock Macromonomers. *J. Am. Chem. Soc.* **2016**, *138* (36), 11501–11504.
416 (4) Li, Z.; Tang, M.; Liang, S.; Zhang, M.; Biesold, G. M.; He, Y.; Hao, S.-M.; Choi, W.; Liu,
417   Y.; Peng, J.; Lin, Z. Bottlebrush Polymers: From Controlled Synthesis, Self-Assembly,
418   Properties to Applications. *Prog. Polym. Sci.* **2021**, *116*, 101387.
419 (5) Bichler, K. J. *Morphology and Dynamics of Bottlebrush Polymers*; Springer Nature, 2021.
420 (6) Sveinbjörnsson, B. R.; Weitekamp, R. A.; Miyake, G. M.; Xia, Y.; Atwater, H. A.; Grubbs,
421   R. H. Rapid Self-Assembly of Brush Block Copolymers to Photonic Crystals. *Proc. Natl.*
422   *Acad. Sci. U. S. A.* **2012**, *109* (36), 14332–14336.
423 (7) Miyake, G. M.; Weitekamp, R. A.; Piunova, V. A.; Grubbs, R. H. Synthesis of Isocyanate-
424   Based Brush Block Copolymers and Their Rapid Self-Assembly to Infrared-Reflecting
425   Photonic Crystals. *J. Am. Chem. Soc.* **2012**, *134* (34), 14249–14254.
426 (8) Liberman-Martin, A. L.; Chu, C. K.; Grubbs, R. H. Application of Bottlebrush Block
427   Copolymers as Photonic Crystals. *Macromol. Rapid Commun.* **2017**, *38* (13).
428   https://doi.org/10.1002/marc.201700058.
429 (9) Chae, C.-G.; Yu, Y.-G.; Seo, H.-B.; Kim, M.-J.; Grubbs, R. H.; Lee, J.-S. Experimental
430   Formulation of Photonic Crystal Properties for Hierarchically Self-Assembled POSS–
431   Bottlebrush Block Copolymers. *Macromolecules* **2018**, *51* (9), 3458–3466.

432 (10) Daniel, W. F. M.; Burdyńska, J.; Vatankhah-Varnoosfaderani, M.; Matyjaszewski, K.;
433   Paturej, J.; Rubinstein, M.; Dobrynin, A. V.; Sheiko, S. S. Solvent-Free, Supersoft and
434   Superelastic Bottlebrush Melts and Networks. *Nat. Mater.* **2016**, *15* (2), 183–189.
435 (11) Vatankhah-Varnosfaderani, M.; Daniel, W. F. M.; Everhart, M. H.; Pandya, A. A.; Liang,
436   H.; Matyjaszewski, K.; Dobrynin, A. V.; Sheiko, S. S. Mimicking Biological Stress–Strain
437   Behaviour with Synthetic Elastomers. *Nature* **2017**, *549* (7673), 497–501.
438 (12) Vatankhah-Varnosfaderani, M.; Keith, A. N.; Cong, Y.; Liang, H.; Rosenthal, M.; Sztucki,
439   M.; Clair, C.; Magonov, S.; Ivanov, D. A.; Dobrynin, A. V.; Sheiko, S. S. Chameleon-like
440   Elastomers with Molecularly Encoded Strain-Adaptive Stiffening and Coloration. *Science*
441   **2018**, *359* (6383), 1509–1513.
442 (13) Seong, H.-G.; Chen, Z.; Emrick, T.; Russell, T. Assembly Behavior of Bottlebrush Random
443   Copolymers at the Water/Toluene Interface; 2022; Vol. 2022, p D19.013.
444 (14) Seong, H.-G.; Fink, Z.; Chen, Z.; Emrick, T.; Russell, T. P. Bottlebrush Polymers at Liquid
445   Interfaces: Assembly Dynamics, Mechanical Properties, and All-Liquid Printed Constructs.
446   *ACS Nano* **2023**, *17* (15), 14731–14741.
447 (15) Kelly, M. T.; Chen, Z.; Russell, T. P.; Zhao, B. Amphiphilic Heterografted Molecular
448   Bottlebrushes with Tertiary Amine-containing Side Chains as Efficient and Robust PH-
449   responsive Emulsifiers. *Angew. Chem. Weinheim Bergstr. Ger.* **2023**.
450   https://doi.org/10.1002/ange.202315424.
451 (16) Chen, Z.; Seong, H.-G.; Hu, M.; Gan, X.; Ribbe, A. E.; Ju, J.; Wang, H.; Doucet, M.;
452   Emrick, T.; Russell, T. P. Janus Bottlebrush Compatibilizers. *Soft Matter* **2024**, *20* (7),
453   1554–1564.
454 (17) Seong, H.-G.; Jin, Z.; Chen, Z.; Hu, M.; Emrick, T.; Russell, T. P. Bottlebrush Block
455   Copolymers at the Interface of Immiscible Liquids: Adsorption and Lateral Packing. *J. Am.*
456   *Chem. Soc.* **2024**, *146* (19), 13000–13009.
457 (18) Barteau, K. P.; Wolffs, M.; Lynd, N. A.; Fredrickson, G. H. Allyl Glycidyl Ether-Based
458   Polymer Electrolytes for Room Temperature Lithium Batteries. *Macromolecules* **2013**.
459 (19) Yin, X.; Qiao, Y.; Gadinski, M. R.; Wang, Q.; Tang, C. Flexible Thiophene Polymers: A
460   Concerted Macromolecular Architecture for Dielectrics. *Polym. Chem.* **2016**, *7* (17), 2929–
461   2933.
462 (20) Zhang, T.; Wang, Y.; Ma, X.; Hou, C.; Lv, S.; Jia, D.; Lu, Y.; Xue, P.; Kang, Y.; Xu, Z. A
463   Bottlebrush-Architectured Dextran Polyprodrug as an Acidity-Responsive Vector for
464   Enhanced Chemotherapy Efficiency. *Biomater Sci* **2020**, *8* (1), 473–484.
465 (21) Han, W.; Byun, M.; Zhao, L.; Rzayev, J.; Lin, Z. Controlled Evaporative Self-Assembly of
466   Hierarchically Structured Bottlebrush Block Copolymer with Nanochannels. *J. Mater.*
467   *Chem.* **2011**, *21* (37), 14248–14253.
468 (22) Hong, S. W.; Gu, W.; Huh, J.; Sveinbjornsson, B. R.; Jeong, G.; Grubbs, R. H.; Russell, T.
469   P. On the Self-Assembly of Brush Block Copolymers in Thin Films. *ACS Nano* **2013**, *7*
470   (11), 9684–9692.
471 (23) Aviv, Y.; Altay, E.; Burg, O.; Müller, M.; Rzayev, J.; Shenhar, R. Bottlebrush Block
472   Copolymer Assembly in Ultraconfined Films: Effect of Substrate Selectivity.
473   *Macromolecules* **2021**, *54* (5), 2079–2089.

474 (24) Gu, W.; Huh, J.; Hong, S. W.; Sveinbjornsson, B. R.; Park, C.; Grubbs, R. H.; Russell, T. P.
475   Self-Assembly of Symmetric Brush Diblock Copolymers. *ACS Nano* **2013**, *7* (3), 2551–
476   2558.
477 (25) Gai, Y.; Song, D.-P.; Yavitt, B. M.; Watkins, J. J. Polystyrene-Block-Poly(Ethylene Oxide)
478   Bottlebrush Block Copolymer Morphology Transitions: Influence of Side Chain Length and
479   Volume Fraction. *Macromolecules* **2017**, *50* (4), 1503–1511.
480 (26) Bolton, J.; Rzayev, J. Synthesis and Melt Self-Assembly of PS–PMMA–PLA Triblock
481   Bottlebrush Copolymers. *Macromolecules* **2014**, *47* (9), 2864–2874.
482 (27) Chen, Z.; Steinmetz, C.; Hu, M.; Coughlin, E. B.; Wang, H.; Heller, W. T.; Bras, W.;
483   Russell, T. P. Star Block Copolymers at Homopolymer Interfaces: Conformation and
484   Compatibilization. *Macromolecules* **2023**, *56* (20), 8308–8322.
485 (28) Chen, Z.; Ribbe, A. E.; Steinmetz, C.; Coughlin, E. B.; Hu, M.; Gan, X.; Russell, T. P.
486   Phase Behavior of Charged Star Block Copolymers at Fluids Interface. *Angew. Chem. Int.
487   Ed Engl.* **2024**, *63* (11), e202400127.
488 (29) Kripotou, S.; Psylla, C.; Kyriakos, K.; Raftopoulos, K. N.; Zhao, J.; Zhang, G.; Pispas, S.;
489   Papadakis, C. M.; Kyritsis, A. Structure and Crystallization Behavior of Poly(Ethylene
490   Oxide) (PEO) Chains in Core–Shell Brush Copolymers with Poly(Propylene Oxide)-Block-
491   Poly(Ethylene Oxide) Side Chains. *Macromolecules* **2016**, *49* (16), 5963–5977.
492 (30) Hsieh, H. W. S.; Post, B.; Morawetz, H. A Crystallographic Study of Polymers Exhibiting
493   Side-chain Crystallization. *J. Polym. Sci. Polym. Phys. Ed.* **1976**, *14* (7), 1241–1255.
494 (31) Müller, A. J.; Balsamo, V.; Arnal, M. L. Nucleation and Crystallization in Diblock and
495   Triblock Copolymers. In *Block Copolymers II*; Abetz, V., Ed.; Springer Berlin Heidelberg:
496   Berlin, Heidelberg, 2005; pp 1–63.
497 (32) He, W.-N.; Xu, J.-T. Crystallization Assisted Self-Assembly of Semicrystalline Block
498   Copolymers. *Prog. Polym. Sci.* **2012**, *37* (10), 1350–1400.
499 (33) Zhu, L.; Cheng, S. Z. D.; Calhoun, B. H.; Ge, Q.; Quirk, R. P.; Thomas, E. L.; Hsiao, B. S.;
500   Yeh, F.; Lotz, B. Phase Structures and Morphologies Determined by Self-Organization,
501   Vitrification, and Crystallization: Confined Crystallization in an Ordered Lamellar Phase of
502   PEO-b-PS Diblock Copolymer. *Polymer* **2001**, *42* (13), 5829–5839.
503 (34) Sun, H.; Yu, D. M.; Shi, S.; Yuan, Q.; Fujinami, S.; Sun, X.; Wang, D.; Russell, T. P.
504   Configurationally Constrained Crystallization of Brush Polymers with Poly(Ethylene
505   Oxide) Side Chains. *Macromolecules* **2019**, *52* (2), 592–600.
506 (35) Seong, H.-G.; Chen, Z.; Emrick, T.; Russell, T. P. Reconfiguration and Reorganization of
507   Bottlebrush Polymer Surfactants. *Angew. Chem. Int. Ed Engl.* **2022**, *61* (19), e202200530.
508 (36) Cochran, E. W.; Morse, D. C.; Bates, F. S. Design of ABC Triblock Copolymers near the
509   ODT with the Random Phase Approximation. *Macromolecules* **2003**, *36* (3), 782–792.
510 (37) Luo, Y.; Kim, B.; Montarnal, D.; Mester, Z.; Pester, C. W.; McGrath, A. J.; Hill, G.;
511   Kramer, E. J.; Fredrickson, G. H.; Hawker, C. J. Improved Self-Assembly of
512   Poly(Dimethylsiloxane-b -Ethylene Oxide) Using a Hydrogen-Bonding Additive. *J. Polym.
513   Sci. A Polym. Chem.* **2016**, *54* (14), 2200–2208.
514 (38) Fredrickson, G. *The Equilibrium Theory of Inhomogeneous Polymers*; Oxford University
515   Press, 2005.
516 (39) Leibler, L. Theory of Microphase Separation in Block Copolymers. *Macromolecules* **1980**,
517   *13* (6), 1602–1617.

518 (40) Chan, J. M.; Kordon, A. C.; Zhang, R.; Wang, M. Direct Visualization of Bottlebrush
519   Polymer Conformations in the Solid State. *Proc. Natl. Acad. Sci. U. S. A.* **2021**, *118* (40).
520   https://doi.org/10.1073/pnas.2109534118.
521 (41) Mei, H.; Mahalik, J. P.; Lee, D.; Laws, T. S.; Terlier, T.; Stein, G. E.; Kumar, R.; Verduzco,
522   R. Understanding Interfacial Segregation in Polymer Blend Films with Random and Mixed
523   Side Chain Bottlebrush Copolymer Additives. *Soft Matter* **2021**, *17* (40), 9028–9039.